China Ocean Eng., 2022, Vol. 36, No. 2, P. 191–207
DOI: https://doi.org/10.1007/s13344-022-0015-x, ISSN 0890-5487
http://www.chinaoceanengin.cn/ E-mail: coe@nhri.cn

Numerical Simulations of Coastal Overwash Using A Phase-Averaged Wave−Current−Sediment Transport Model

LI Song-zhe[a], JI Chao[b, *], ZHANG Qing-he[a], CHEN Tong-qing[a]

[a] State Key Laboratory of Hydraulic Engineering Simulation and Safety, Tianjin University, Tianjin 300350, China
[b] Key Laboratory of Engineering Sediment, Tianjin Research Institute for Water Transport Engineering, Ministry of Transport, Tianjin 300456, China

Received September 24, 2021; revised January 1, 2022; accepted February 8, 2022

Abstract

Coastal overwash is a natural phenomenon that commonly occurs during storm events and can cause considerable changes in nearshore morphology within a short time. In this study, a complete set of empirical overwash transport algorithms is developed and introduced into a phase-averaged wave-current-sediment transport coupling model that integrates the Finite-Volume Community Ocean Model (FVCOM) and the Simulating Waves Nearshore (SWAN) model. The resulting morphological evolution model can simulate coastal overwash. Validation against the data obtained from multiple sets of laboratory overwash experiments demonstrates that the model performs relatively well in simulating morphological changes caused by runup overwash and inundation overwash under different hydrodynamic and beach profile conditions. The sensitivity of each empirical coefficient in the overwash transport algorithms is comprehensively analyzed. The effects of each coefficient on the output of the model are discussed, and a recommended value range is provided for each coefficient.

Key words: wave-current coupling, phase-averaged model, overwash, wave runup, morphological evolution

Citation: Li, S. Z., Ji, C., Zhang, Q. H., Chen, T. Q., 2022. Numerical simulations of coastal overwash using a phase-averaged wave−current−sediment transport model. China Ocean Eng., 36(2): 191–207, doi: https://doi.org/10.1007/s13344-022-0015-x

1 Introduction

Coastal overwash refers to the landward migration of water (including the sediment that it carries) propelled by waves and currents flowing over the crest of a coastal barrier or dune, and it usually occurs during a storm event (Donnelly, 2008; Matias et al., 2010). Overwash may cause erosion, flooding, sediment intrusion, and barrier breaching (Cao et al., 2020; Kupfer et al., 2020; Wang et al., 2020), so it is a relatively hazardous process, making it vital to study overwash and overwash-induced morphological changes.

There are two main modes of overwash in coastal zones (Fig. 1). (a) Runup overwash (RO) occurs when the mean water level height S (including the astronomical tide, the storm surge, and the wave setup) does not exceed the dune crest height z_C (i.e., $S \leqslant z_C$) but the wave runup height R is larger than z_C ($R > z_C$). (b) Inundation overwash (IO) occurs when $S > z_C$. These two modes of overwash may occur either separately during different stages of a storm surge or concurrently at different coastal locations. See the review by Donnelly et al. (2006) for the details of these two modes of overwash.

Because of its importance, many researchers have studied overwash through field observations, laboratory experiments, and numerical simulations. Stockdon et al. (2009), Matias et al. (2010), and Carruthers et al. (2013) conducted field investigations on morphological changes and the extents of erosion and deposition caused by overwash, as well as its reach of influence, using different measurement methods. Hancock and Kobayashi (1994) experimentally examined overwash under the action of waves with different periods. They measured wave overtopping rates, sediment transport rates, and morphological profiles and compared the measurements with the results yielded by the empirical equations. Through a series of wave flume experiments, Figlus et al. (2009, 2011) studied the overwash of three types of dunes with different morphologies and discussed their overwash resistance. Donnelly (2008) conducted RO experiments under different hydrodynamic conditions with a focus on the hydrodynamic and morphological changes at the crest and onshore sides of dunes. Matias et al. (2012, 2013)

Foundation item: This study is financially supported by the National Natural Science Foundation of China (Grant Nos. U1906231 and 51509183), the Tianjin Transportation Science and Technology Development Plan Project (Grant No. 2020-12), and the Fundamental Research Funds for the Central Public Welfare Research Institutes (Grant No. TKS20200410).

*Corresponding author. E-mail: jichao@tiwte.ac.cn

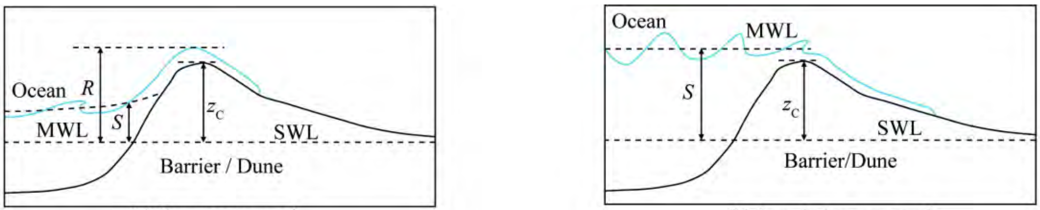

(a) Runup overwash (b) Inundation overwash

Fig. 1. Two overwash modes on the coast: (a) runup overwash and (b) inundation overwash, where the mean water level (MWL) includes the effects of astronomical tide, storm surge, and wave setup; the still water level (SWL) occurs in the absence of waves; R is runup height above SWL; S is the MWL height above the SWL; and z_C is the barrier or dune crest height above the SWL.

conducted a series of RO experiments on gravelly and sandy beaches in a large-scale water flume, summarized the overwash threshold, and analyzed in detail the height, flow, and reach of influence of overtopping water and the morphological changes it caused. These field observations and experimental studies provide an important basis for an in-depth understanding of the overwash process.

Numerical simulations have also examined the effects of overwash. Srinivas and Dean (1996) developed an onshore/offshore profile model that simulates IO-induced coastal profile changes. Larson and Kraus (1989) and Larson et al. (2004b) established a storm-induced beach change (SBEACH) model based on the concept of equilibrium sediment transport, to which they later added an overwash algorithm to simulate beach profile changes under storm action. Kobayashi (2013, 2016) developed a cross-shore numerical model, termed CSHORE, that calculates the wave runup and RO transport processes in the intermittently wet and dry zone through probability functions. Primarily used to simulate beach profile changes, these models do not account for the sediment transport and topography variation in the alongshore direction. Roelvink et al. (2009) established a two-dimensional horizontal (2DH) model, termed XBeach, that considers the infragravity wave runup process and the relevant sediment transport mechanism, and it may be better suited for predicting beach deformation with alongshore-varying hydrodynamic and topographic conditions. Many researchers have employed XBeach to simulate overwash transport and coastal morphological changes during storm events (McCall et al., 2010; Harris et al., 2020). XBeach is more computationally expensive than the common phase-averaged models because it needs to calculate the equations of motion for flow and sediment at the wave-group time scale, so it is mainly applicable to spatial scales on the order of 10 km×10 km (van Dongeren et al., 2017). In addition, XBeach usually does not consider the overwash caused by short waves in its 2DH applications (McCall et al., 2010, 2014).

Discontinuous wave overtopping is an important dynamic mechanism of overwash. As a result, the common three-dimensional (3D) phase-averaged morphological models (e.g., the Regional Ocean Modeling System (ROMS); Estuarine, Coastal Ocean Model with Sediment Transport (ECOMSED); and Delft3D) cannot calculate the wave-dominated overwash. Calculating the equations of motion for water and sediment at the wave-group or short-wave time scale increases the computational cost of a model and hinders its application to relatively large spatial scales (van Dongeren et al., 2017). In this study, a set of empirical overwash algorithms was developed based on a 3D phase-averaged wave-current-sediment transport coupling model to describe net overwash transport over many wave periods. On this basis, a morphological evolution model that could reasonably simulate overwash was established. The rest of this paper is organized as follows. Section 2 introduces in detail the relevant models, including the hydrodynamic, wave, and sediment models, and the involved overwash transport algorithms. Section 3 examines the reliability of the beach evolution model established in this study against a series of experimental data. Section 4 analyzes the sensitivity of the empirical coefficients in the overwash transport algorithms. Section 5 discusses the conclusions.

2 Model description

2.1 Model framework

Fig. 2 shows the framework of the wave-current-sediment transport coupling model (including overwash algorithms) established in this study. The model consists of four parts, namely, a hydrodynamic model (i.e., the Finite-Volume Community Ocean Model (FVCOM)), a wave model (i.e., the Simulating Waves Nearshore (SWAN) model), a sediment model, and a morphological evolution model. FVCOM provides water levels and depth-averaged velocities to the SWAN model, while SWAN provides wave

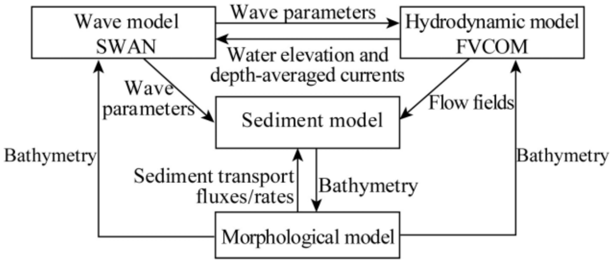

Fig. 2. Model framework.

parameters, including the significant wave height, wave direction, spectral peak period, wave length, fraction of breaking waves, near-bottom orbital velocity, and near-bottom wave period (defined as 2π times the ratio of the bottom excursion amplitude to the orbital velocity) to the FVCOM. The wave and hydrodynamic models are coupled through a Model Coupling Toolkit (MCT) coupler (Chen et al., 2018; Ji et al., 2018). The sediment model calculates the suspended load and bedload transport based on the flow conditions and wave parameters.

We also develop an overwash module in the sediment model to calculate overwash transport rates using empirical equations. The sediment transport fluxes/rates (i.e., the erosion and deposition fluxes of the suspended load as well as the bedload and overwash transport rates) yielded by the sediment model are used to calculate beach evolution, while the morphological changes calculated by the morphological model are fed back to the hydrodynamic, wave, and sediment models to couple wave-current dynamics, sediment transport, and morphological evolution.

2.2 Hydrodynamic model

FVCOM (Chen et al., 2003, 2007) is used to calculate hydrodynamic values. Its equations of continuity and momentum can be expressed as follows:

$$\frac{\partial \eta}{\partial t}+\frac{\partial Du}{\partial x}+\frac{\partial Dv}{\partial y}+\frac{\partial w}{\partial \varsigma}=0; \tag{1}$$

$$\begin{aligned}\frac{\partial uD}{\partial t}+\frac{\partial u^2D}{\partial x}+\frac{\partial uvD}{\partial y}+\frac{\partial uw}{\partial \varsigma}-fvD={}&-gD\frac{\partial \eta}{\partial x}-\\&\frac{D}{\rho_0}\frac{\partial p_{\rm a}}{\partial x}-\frac{gD}{\rho_0}\left(\int_{\varsigma}^{0}D\frac{\partial \rho}{\partial x}{\rm d}\varsigma-\frac{\partial D}{\partial x}\int_{\varsigma}^{0}\varsigma\frac{\partial \rho}{\partial \varsigma}{\rm d}\varsigma\right)+\\&\frac{1}{D}\frac{\partial}{\partial \varsigma}\left(K_{\rm m}\frac{\partial u}{\partial \varsigma}\right)+DF_x-\frac{\partial DS_{xx}}{\partial x}-\frac{\partial DS_{yx}}{\partial y}+\\&\frac{\partial S_{px}}{\partial \varsigma}-\frac{\partial DR_{xx}}{\partial x}-\frac{\partial DR_{yx}}{\partial y};\end{aligned} \tag{2}$$

$$\begin{aligned}\frac{\partial vD}{\partial t}+\frac{\partial uvD}{\partial x}+\frac{\partial v^2D}{\partial y}+\frac{\partial vw}{\partial \varsigma}+fuD={}&-gD\frac{\partial \eta}{\partial y}-\\&\frac{D}{\rho_0}\frac{\partial p_{\rm a}}{\partial y}-\frac{gD}{\rho_0}\left(\int_{\varsigma}^{0}D\frac{\partial \rho}{\partial y}{\rm d}\varsigma-\frac{\partial D}{\partial y}\int_{\varsigma}^{0}\varsigma\frac{\partial \rho}{\partial \varsigma}{\rm d}\varsigma\right)+\\&\frac{1}{D}\frac{\partial}{\partial \varsigma}\left(K_{\rm m}\frac{\partial v}{\partial \varsigma}\right)+DF_y-\frac{\partial DS_{xy}}{\partial x}-\frac{\partial DS_{yy}}{\partial y}+\\&\frac{\partial S_{py}}{\partial \varsigma}-\frac{\partial DR_{xy}}{\partial x}-\frac{\partial DR_{yy}}{\partial y},\end{aligned} \tag{3}$$

where $D=h+\eta$ is the total water depth; h is the bottom depth; η is the water surface elevation (h and η are relative to the SWL in this study); $\varsigma=(z-\eta)/D$ is the vertical coordinate; u, v, and w are the velocity components in the x-, y-, and ς-directions, respectively; t is time; f is the Coriolis coefficient; g is the gravitational acceleration; ρ is the total density; ρ_0 is the reference density; $p_{\rm a}$ is the atmospheric pressure at the sea surface; $K_{\rm m}$ is the vertical eddy viscosity coefficient; F_x and F_y are the horizontal momentum diffusion terms; R_{xx}, R_{yx}, R_{xy}, and R_{yy} are the wave surface roller terms, which are calculated using the formulations given by Svendsen (1984); S_{xx}, S_{yx}, S_{xy}, and S_{yy} are the horizontal radiation stress terms; and S_{px} and S_{py} are the vertical radiation stress terms. The 3D radiation stress terms are calculated using the new formulations derived by Ji et al. (2017, 2019) that account for the beach slope effects.

2.3 Wave model

Waves are simulated in this study using the SWAN model (Booij et al., 1999), whose governing equation is a spectral wave action balance equation that contains a source-and-sink term:

$$\frac{\partial}{\partial t}N+\frac{\partial}{\partial x}C_xN+\frac{\partial}{\partial y}C_yN+\frac{\partial}{\partial \sigma}C_\sigma N+\frac{\partial}{\partial \theta}C_\theta N=\frac{S_{\rm tot}}{\sigma}, \tag{4}$$

where N is the spectral wave action density; σ is the relative wave frequency; θ is the wave propagation direction; C_x and C_y are the propagation velocities in the x- and y-directions, respectively; C_σ and C_θ are the propagation velocities in the σ- and θ-spaces, respectively; and $S_{\rm tot}$ is the source-and-sink term that represents the generation, dissipation, and redistribution of the wave energy. In this study, $S_{\rm tot}$ mainly includes the dissipations due to bottom friction and depth-induced breaking. The former can be expressed as follows:

$$S_{\rm ds,b}=-C_{\rm b}\frac{\sigma^2}{g^2\sinh^2kD}E(\sigma,\theta), \tag{5}$$

where $C_{\rm b}$ is a bottom friction coefficient, k is the wavenumber, and $E(\sigma,\theta)$ is the energy density spectrum. The dissipation by depth-induced wave breaking for a spectral component per unit time is calculated in SWAN with

$$S_{\rm ds,br}(\sigma,\theta)=\frac{D_{\rm tot}}{E_{\rm tot}}E(\sigma,\theta), \tag{6}$$

where $E_{\rm tot}$ is the total wave energy and $D_{\rm tot}$ is the mean rate of energy dissipation per unit horizontal area due to wave breaking, which is calculated as follows:

$$D_{\rm tot}=-\frac{1}{4}\alpha_{\rm BJ}Q_{\rm b}\left(\frac{\bar{\sigma}}{2\pi}\right)H_{\rm max}^2, \tag{7}$$

where $\alpha_{\rm BJ}=1$ in SWAN, $\bar{\sigma}$ is the mean frequency, and $Q_{\rm b}$ is the fraction of breaking waves that is determined by

$$\frac{1-Q_{\rm b}}{\ln Q_{\rm b}}=-8\frac{E_{\rm tot}}{H_{\rm max}^2}, \tag{8}$$

where $H_{\rm max}=\gamma_{\rm b}D$ is the maximum wave height, in which the wave breaker index $\gamma_{\rm b}$ can be calculated following Goda (2009):

$$\gamma_{\rm b}=\frac{A}{D/L_0}\left\{1-\exp\left[-1.5\frac{\pi D}{L_0}\left(1+15\tan^{4/3}\beta\right)\right]\right\}, \tag{9}$$

where L_0 is the wavelength in deep water, β is the angle of the beach slope, and A is an empirical coefficient calculated following Ji et al. (2018):

$$A = 0.228 \times \left(\frac{H_0}{L_0}\right)^{0.108}. \tag{10}$$

In this study, Eqs. (9) and (10) are used to determine the breaker index based on the wave parameters, water depth, and beach slope, such that the SWAN model can provide accurate predictions of nearshore wave breaking without manually adjusting the parameters of the breaker index (Ji et al., 2018).

2.4 Sediment model

2.4.1 *Suspended transport*

The suspended transport is calculated using the following convection–diffusion equation:

$$\frac{\partial cD}{\partial t} + \frac{\partial ucD}{\partial x} + \frac{\partial vcD}{\partial y} + \frac{\partial (w - w_s)c}{\partial \varsigma} = D\frac{\partial}{\partial x}\left(A_h \frac{\partial c}{\partial x}\right) + D\frac{\partial}{\partial y}\left(A_h \frac{\partial c}{\partial y}\right) + \frac{1}{D}\frac{\partial}{\partial \varsigma}\left(K_h \frac{\partial c}{\partial \varsigma}\right), \tag{11}$$

where c is the sediment concentration, A_h is the horizontal diffusion coefficient (which is set to be equal to the horizontal eddy viscosity coefficient of the flow in the model), K_h is the vertical sediment diffusion coefficient that includes the wave effects based on the method used by van Rijn (2007), and w_s is the sediment fall velocity that is calculated using the equation given by van Rijn (1993). At the free surface, the vertical diffusive flux is zero, and the following boundary condition is used:

$$-K_h \frac{\partial c}{\partial z} - w_s c = 0. \tag{12}$$

The following condition is applied at the bottom (Cao et al., 2021):

$$-K_h \frac{\partial c}{\partial z} - w_s c = E_s - D_s, \tag{13}$$

where E_s and D_s are the erosion and deposition fluxes, respectively, and are calculated based on methods used by Lesser et al. (2004) and van Rijn (2007).

2.4.2 *Bedload transport*

Bedload transport is calculated using the equation given by Soulsby and Damgaard (2005). The dimensionless bedload transport rate vector under combined wave-current action can be decomposed into two components, one along the current direction and one perpendicular to the current direction:

$$\boldsymbol{\Phi} = \left(\Phi_a,\ \Phi_p\right). \tag{14}$$

The component of the dimensionless bedload transport rate along the current direction is

$$\Phi_a = \max(\Phi_{a1},\ \Phi_{a2}), \tag{15}$$

where

$$\Phi_{a1} = A_2 \theta_m^{1/2} (\theta_m - \theta_{cr}); \tag{16}$$

$$\Phi_{a2} = A_2 (0.9534 + 0.1907 \cos 2\varphi)\, \theta_w^{1/2} \theta_m + A_2 \left(0.229 \varDelta \theta_w^{3/2} \cos\varphi\right), \tag{17}$$

where A_2 is an empirical coefficient (usually set to 12.0), φ is the angle between the wave and current, $\varDelta$ is the wave asymmetry coefficient (set to 0.2), θ_m is the period-averaged Shields parameter under combined wave and current action, θ_w is the Shields parameter under wave action, and θ_{cr} is the critical Shields parameter. See Soulsby (1997) for the calculation method of each of these Shields parameters.

The component of the dimensionless bedload transport rate perpendicular to the current direction is expressed as follows:

$$\Phi_p = A_2 \frac{0.1907 \theta_w^2}{\theta_w^{3/2} + 1.5\theta_w^{3/2}} (\theta_m \sin 2\varphi + 1.2 \varDelta \theta_w \sin\varphi). \tag{18}$$

The final bedload transport rate vector can be expressed as:

$$\boldsymbol{q}_b = \rho_s \boldsymbol{\Phi} \sqrt{(s-1) g d_{50}}\, d_{50}, \tag{19}$$

where ρ_s is the sediment density, $s = \rho_s / \rho$ is the relative density, and d_{50} is the median sediment particle diameter.

2.4.3 *Overwash transport*

The two modes of coastal overwash, RO and IO, involve different sediment transport mechanisms. Hence, it is necessary to develop an algorithm to calculate the sediment transport rate in each mode.

2.4.3.1 *Runup overwash transport*

To establish an RO transport algorithm, a coastal zone is divided into three zones in the onshore/offshore direction, namely, a swash zone, a barrier/dune crest zone, and a back-

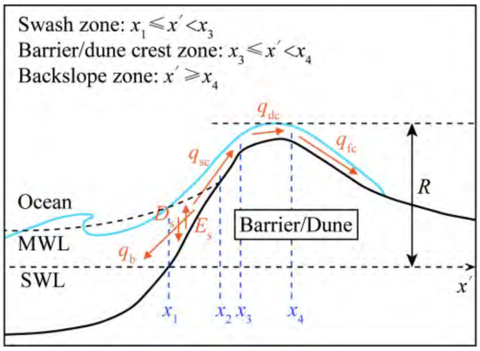

Fig. 3. Three zones described in the runup overwash algorithm, in which the x'-axis points onshore, x_1 represents the junction of the SWL and the beach face, x_2 represents the junction of the MWL and the beach face, x_3 represents the junction of the swash zone and the barrier/dune crest zone, x_4 represents the junction of the barrier/dune crest zone and the backslope zone, q_{sc} is the cross-shore runup overwash transport rate in the swash zone ($x_1 \leqslant x' < x_3$), q_{dc} is the cross-shore runup overwash transport rate over the barrier/dune crest ($x_3 \leqslant x' < x_4$), q_{fc} is the cross-shore runup overwash transport on the backslope of barrier/dune ($x' \geqslant x_4$), q_b is the bedload transport rate below the MWL ($x' \leqslant x_2$), and E_s and D_s are the erosion and deposition fluxes for suspended load transport below the MWL ($x' \leqslant x_2$), respectively.

slope zone (Fig. 3). The three zones are identified in the model based on the beach slope gradient. Specifically, a slope gradient parameter $\tan\beta_0$ with a default value of 0.1 is introduced to determine the type of each zone at $x'\geqslant x_1$. If the slope gradient $\tan\beta_{x'}$ in the onshore/offshore direction (an upslope gradient is deemed positive, and a downslope gradient is deemed negative) is larger than $\tan\beta_0$, the zone is deemed the swash zone; if $\left|\tan\beta_{x'}\right|\leqslant\tan\beta_0$, the zone is deemed the barrier/dune crest zone; and if $\tan\beta_{x'}<-\tan\beta_0$, the zone is deemed the backslope zone. This identification approach can adapt to the dynamic changes at the boundaries of different zones during dune erosion evolution. Note that this simple slope index may be invalid on beaches with very complex variations in slope. In this case, the $\tan\beta_0$ value may need to be adjusted, or a special identification method may be required, depending on the specific conditions.

The method used to calculate the RO transport rate in each of the three zones is described below.

(1) Swash zone

Previous studies have investigated the sediment transport for the swash zone under non-RO conditions, but most of them are based on phase-resolving methods (Zhu and Dodd, 2013; Hu et al., 2015; Deng et al., 2016; Li et al., 2017). In this study, an RO transport equation is derived for the swash zone based on the phase-averaged method used by Larson et al. (2004a). First, the equation developed by Madsen (1991) to calculate the instantaneous sediment transport rate is introduced:

$$\frac{q(t)}{\rho_{\rm s}\sqrt{(s-1)gd_{50}}\,d_{50}}=\frac{8}{1+\dfrac{\tan\beta}{\tan\phi_{\rm m}}}\left(|\theta(t)|-\theta_{\rm cr}\right)^{3/2}\frac{\tau_{\rm b}(t)}{|\tau_{\rm b}(t)|},\tag{20}$$

where $\tan\beta$ is the local slope gradient, $\phi_{\rm m}$ is the angle of internal friction of the sediment (set to 33°), $\theta(t)$ is the instantaneous Shields parameter, and $\tau_{\rm b}(t)$ is the instantaneous bed shear stress.

It is relatively difficult to determine the respective contributions of the bedload (or sheetflow) and suspended load to the sediment transport in the swash zone. Although Eq. (20) is mainly used to calculate the bedload transport rate, similar equations based on the bed shear stress are also used to predict the total sediment transport rate $q_{\rm t}$ (Larson et al., 2004a). Therefore, in this study, Eq. (20) is used to calculate the instantaneous $q_{\rm t}$ in the swash zone under the condition that its coefficients can be appropriately adjusted.

Assume that waves propagate onshore along the x'-axis and water does not return once it has overtopped the barrier. Following Larson et al. (2004a), the flow velocity and shear stress in the swash zone are large, so the critical Shields parameter $\theta_{\rm cr}$ in Eq. (20) can be neglected. Then, we can obtain the following expression of the average cross-shore sediment transport rate at a certain location in the swash zone within one wave period if we phase-average Eq. (20):

$$\frac{q_{\rm sc}}{\rho_{\rm s}\sqrt{(s-1)gd_{50}}\,d_{50}}=\frac{\dfrac{8}{T}\displaystyle\int_{t_{\rm s}}^{t_{\rm e}}\left(|\theta(t)|\right)^{3/2}{\rm d}t}{1+\dfrac{\tan\beta_{x'}}{\tan\phi_{\rm m}}},\tag{21}$$

where T is the wave period; $t_{\rm s}$ and $t_{\rm e}$ are the starting and ending time of the water runup process at the given location, respectively; and $t_{\rm e}-t_{\rm s}$ represents the duration of the runup action at this location in a wave period.

Guided by the method of Larson et al. (2004a), the instantaneous flow velocity u at each location can be assumed to be a function of time t:

$$\frac{u}{u_0}=\Gamma\left(\frac{t-t_{\rm s}}{t_0}\right),\tag{22}$$

where $u_0=\sqrt{2g(R-z)}$ is defined as the uprush bore front velocity at height z (relative to the SWL) and $t_0=t_{\rm e}-t_{\rm s}=T\sqrt{1-z/R}$. The following equation gives the empirical relationship between $\theta(t)$ and $u(t)$:

$$|\theta(t)|=\frac{|\tau_{\rm b}(t)|}{\rho(s-1)gd_{50}}=\frac{0.5\rho f_{\rm b}u^2(t)}{\rho(s-1)gd_{50}},\tag{23}$$

where $f_{\rm b}$ is the coefficient of friction. Substituting Eqs. (22) and (23) into Eq. (21) simplifies Eq. (21) to

$$q_{\rm sc}=K_{\rm sc}\rho_{\rm s}\frac{\tan\phi_{\rm m}}{\tan\phi_{\rm m}+\tan\beta_{x'}}\frac{u_0^3}{g}\frac{t_0}{T},\tag{24}$$

where $K_{\rm sc}$ is the empirical coefficient of cross-shore sediment transport in the swash zone. Wave runup height R required for calculating u_0 and t_0/T in Eq. (24) is calculated using the equation given by Stockdon et al. (2006).

Based on the method used by Larson and Wamsley (2007), directly adjusting Eq. (24) yields the following expression of the longshore sediment transport rate in the swash zone:

$$q_{\rm sl}=K_{\rm sl}\rho_{\rm s}\frac{\tan\phi_{\rm m}}{\tan\phi_{\rm m}+\tan\beta_{y'}}\frac{u_0^2v_0}{g}\frac{t_0}{T},\tag{25}$$

where $K_{\rm sl}$ is the empirical coefficient of longshore sediment transport in the swash zone, v_0 is the longshore component of the uprush bore front velocity, and $\tan\beta_{y'}$ is the longshore slope gradient.

(2) Barrier/dune crest zone

Based on Donnelly (2008), the cross-shore sediment transport rate in the barrier/dune crest zone that accounts for the effects of the beach slope can be expressed as follows:

$$q_{\rm dc}=K_{\rm dc}\rho_{\rm s}\frac{\tan\phi_{\rm m}}{\tan\phi_{\rm m}+\tan\beta_{x'}}\frac{u_{\rm D}^3}{g}\frac{t_{\rm D}}{T},\tag{26}$$

where $K_{\rm dc}$ is the empirical coefficient of cross-shore sediment transport in the barrier/dune crest zone, $u_{\rm D}=\sqrt{2g(R-z_{\rm D})}$ is the bore front velocity at the height $z_{\rm D}$ in the barrier/dune crest zone, $t_{\rm D}=T\sqrt{1-z_{\rm D}/R}$ is the duration of overtopping at this location, and $z_{\rm D}$ is the barrier height in the barrier/dune crest zone (relative to the SWL).

The method used to establish Eq. (26) is employed to derive the following final expression of the longshore sediment transport rate in the barrier/dune crest zone:

$$q_{\mathrm{dl}} = K_{\mathrm{dl}}\rho_{\mathrm{s}}\frac{\tan\phi_{\mathrm{m}}}{\tan\phi_{\mathrm{m}}+\tan\beta_{y'}}\frac{u_{\mathrm{D}}^{2}v_{\mathrm{D}}}{g}\frac{t_{\mathrm{D}}}{T}, \tag{27}$$

where K_{dl} is the empirical coefficient of longshore sediment transport in the barrier/dune crest zone and v_{D} is the longshore component of the bore front velocity.

(3) Backslope zone

The cross-shore sediment transport rate in the backslope zone is calculated using the equation given by Larson et al. (2004b):

$$q_{\mathrm{fc}} = \frac{q_{\mathrm{dc}}^{+}}{1+\mu s_{\mathrm{f}}/B_{\mathrm{D}}}, \tag{28}$$

where q_{dc}^{+} is the cross-shore sediment transport rate at the junction of the barrier/dune crest zone and the backslope zone ($x' = x_4$) calculated using Eq. (26), s_{f} is the distance from this junction along the bed surface, μ is an empirical coefficient related to lateral flow spread, and B_{D} is the flow width in the barrier/dune crest zone. Larson et al. (2004b) noted that μ and B_{D} are determined by multiple factors (e.g., local morphology and wave conditions) and are difficult to calibrate, so they recommended that these two parameters be combined. Since the effects of the slope gradient, Eq. (28) can be written as follows:

$$q_{\mathrm{fc}} = \frac{\tan\phi_{\mathrm{m}}q_{\mathrm{dc}}^{+}}{(\tan\phi_{\mathrm{m}}+\tan\beta_{x'})(1+K_{\mathrm{fc}}s_{\mathrm{f}})}, \tag{29}$$

where K_{fc} is the empirical coefficient of cross-shore sediment transport in the backslope zone. Similarly, the following equation is used to calculate the longshore sediment transport rate in the backslope zone:

$$q_{\mathrm{fl}} = \frac{\tan\phi_{\mathrm{m}}q_{\mathrm{dl}}^{+}}{\left(\tan\phi_{\mathrm{m}}+\tan\beta_{y'}\right)(1+K_{\mathrm{fl}}s_{\mathrm{f}})}, \tag{30}$$

where q_{dl}^{+} is the longshore sediment transport rate at the junction of the barrier/dune crest zone and the backslope zone ($x' = x_4$) calculated using Eq. (27) and K_{fl} is the empirical coefficient of longshore sediment transport in the backslope zone.

From the above considerations, the RO transport rates in different zones can be calculated using Eqs. (24), (25), (26), (27), (29), and (30). Theoretically, when $K_{\mathrm{sc}} = K_{\mathrm{dc}}$ and $K_{\mathrm{sl}} = K_{\mathrm{dl}}$, the RO transport rate is continuous at the junction of the swash zone and the barrier/dune crest zone, but we place no strict restrictions on it in this study. The values of coefficients K_{sc} and K_{dc} are discussed in Section 4.1.

Because the sediment transport formulation in the swash zone is empirical, we do not couple the suspended transport, bedload transport, and overwash transport modules. These three modules are calculated separately, but all are fed back by the bed level changes. The transition zone ($x_1 \leqslant x' \leqslant x_2$ in Fig. 3), which includes not only the calculation of sediment transport in the swash zone but also the calculation of suspended and bedload transport, avoids excessive local morphological changes due to sudden variations in the sediment transport rate to some extent.

2.4.3.2 Inundation overwash transport

IO occurs when S on the ocean side of the barrier exceeds z_{C} (Fig. 1b). Guided by the formulation of Donnelly (2008) and the characteristics of IO under wave action, the following equation is used to calculate the onshore/offshore IO transport rate across the beach profile:

$$q_{\mathrm{ic}} = K_{\mathrm{ic}}K_{\mathrm{p}}K_{\mathrm{t}}\rho_{\mathrm{s}}\frac{\tan\phi_{m}}{\tan\phi_{m}+\tan\beta_{x'}}2\sqrt{2g}(R-z)^{3/2}, \tag{31}$$

where K_{ic} is the cross-shore IO transport coefficient, K_{p} is a parameter that characterizes the distribution of the sediment transport rate across the profile, and K_{t} is a parameter that characterizes the variation in the sediment transport rate with the extent of overwash. K_{p} and K_{t} are calculated by the following equations:

$$K_{\mathrm{p}} = \left[\max\left(1-\frac{z_{\mathrm{C}}-z}{h_0},\ 0\right)\right]^{k_1}; \tag{32}$$

$$K_{\mathrm{t}} = \left\{\min\left[\max\left(1+\frac{z_{\mathrm{C}}}{h_0},\ 0\right),\ 1\right]\right\}^{k_2}, \tag{33}$$

where h_0 is the limit depth of IO relative to the SWL and k_1 and k_2 are empirical coefficients.

Previous experimental results of IO under wave action (Wang et al., 2020) show inconsistencies in the distribution of the sediment transport rate and the pattern of morphological changes on the seaward and landward sides of a dune during the overwash process. Hence, in this study, a coastal zone under IO action is simplistically divided into a seaward zone and a landward zone in the onshore/offshore direction (Fig. 4). The junction of the seaward and landward zones ($x' = x_{\mathrm{C}}$) corresponds to the barrier/dune crest point, which varies dynamically during the numerical simulation process. The empirical coefficient k_1 affects the value of K_{p}, which characterizes the distribution of the sediment trans-

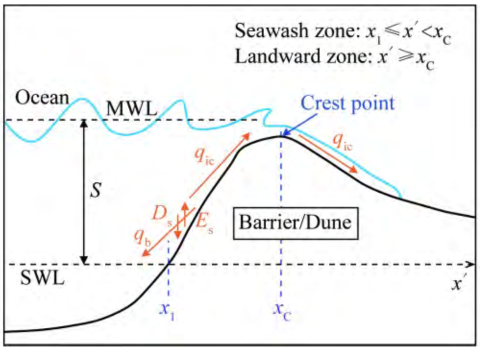

Fig. 4. Two zones described in the inundation overwash algorithm, in which x_{C} represents the junction of the seaward and landward zones and q_{ic} is the cross-shore inundation overwash transport rate.

port rate across the profile. Therefore, different values of k_1 are used to calculate the IO transport rates in the seaward and landward zones. For convenience, k_{1s} and k_{1f} are used to denote k_1 of the seaward and landward zones, respectively. At the dune crest, $z = z_C$ and $K_p = 1$. As a result, while the values of k_1 for the two zones are different, Eq. (31) yields a continuous sediment transport rate q_{ic} near the dune crest (at $x' \approx x_C$). The coefficients K_{ic} and k_2 control the magnitude of the IO-induced sediment transport rate and the overall variation in the sediment transport rate with the overwash progress, respectively, so they remain the same for both zones.

Longshore IO may occur at the barrier in the presence of obliquely incident waves. The following cross-shore and longshore IO transport rates are established based on the overwash transport module established in the previous section and on Eq. (31):

$$q_{ic} = K_{ic} K_p K_t \rho_s \frac{\tan\phi_m}{\tan\phi_m + \tan\beta_{x'}} 2\sqrt{2g}(R-z)^{3/2}\cos\theta; \tag{34}$$

$$q_{il} = K_{il} K_p K_t \rho_s \frac{\tan\phi_m}{\tan\phi_m + \tan\beta_{y'}} 2\sqrt{2g}(R-z)^{3/2}\sin\theta, \tag{35}$$

where θ is the angle between the nearshore wave direction and the normal direction of the coast and K_{il} is the longshore IO sediment transport coefficient.

2.5 Morphological model

The governing equation for morphological evolution can be written as follows:

$$\rho_s(1-p_{or})\frac{\partial z_b}{\partial t} + f_{mor}\left(\frac{\partial q_x}{\partial x} + \frac{\partial q_y}{\partial y} + E_s - D_s\right) = 0, \tag{36}$$

where z_b is the bed level, p_{or} is the porosity, f_{mor} is the morphological acceleration factor, and q_x and q_y are the sums of the bedload and overwash transport rates in the x- and y-directions, respectively. The bed level changes calculated with the above equation are fed back into the wave, hydrodynamic, and sediment models to simulate the full coupling of waves, currents, sediment transport, and morphological evolution (Fig. 2).

3 Model validation

3.1 Case 1: Runup overwash only

Park (2006) conducted RO experiments under different wave conditions in a wave flume (28.0 m long, 1.5 m wide, and 3.0 m deep) in the Hydrolab at Texas A&M University. An experimental case that lasted for a relatively long time and involved relatively notable morphological changes was simulated in this study. The significant wave height H_s and spectral peak period T_p of the incident waves were 0.15 m and 2.0 s, respectively. The waves broke in the form of a plunging breaker on a 1:5 sloped sand berm built of sediment with a d_{50} of 0.15 mm, and this experiment lasted for 1635 s.

Table 1 summarizes the specific values of the RO transport coefficients in this validation case. In the model run, the grid resolution is 0.2 m. The time steps for FVCOM and SWAN are 0.005 and 10 s, respectively, and the time interval for information exchange between the two models is 10 s. Figs. 5a and 5b give the model-calculated values of the initial H_s and wave-induced undertow velocity. The simulated wave-breaking point occurs at $x \approx 23.0$ m, the undertow is relatively strong within the wave-breaking zone, and the near-bottom velocity is relatively low outside the wave-breaking zone. Figs. 5c and 5d show the distribution of the calculated time-averaged total sediment transport rate q_t and compare the simulated and measured beach profiles, respectively. In the zone at $x \leqslant 24.7$ m, sediment is overall transported offshore under the action of undertow. The time-averaged q_t is mainly offshore and reaches its maximum at the turning point A ($x \approx 23.8$ m), beyond which it decreases rapidly. As a result, the simulated profile of the zone at 23.8 m < x < 24.7 m exhibits an eroded morphology, while deposition and its resulting underwater sandbar are visible at 22.7 m < x < 23.8 m. In the zone at x > 24.7 m, sediment is largely transported onshore under the RO action, and the time-averaged q_t is mainly onshore, peaking around the turning point B ($x \approx 26.4$ m). Correspondingly, the swash and barrier/dune crest zones at x < 26.4 m are mostly eroded, while slight deposition takes place in the backslope zone at x > 26.4 m.

For all cases, the model performances were quantified by statistical parameters, including the root mean squared error (*RMSE*) and correlation coefficient (*CC*):

$$RMSE = \sqrt{\frac{1}{n}\sum_{i=1}^{n}(x_i - y_i)^2}; \tag{37}$$

Table 1 Empirical coefficient values in the overwash algorithm for the validation cases

Empirical coefficients	Case 1	Case 2-BD	Case 3-WD	Case 2-SD	Case 3
K_{sc}	1.8×10^{-4}	4.6×10^{-5}	2.0×10^{-5}	3.6×10^{-5}	–
K_{dc}	2.4×10^{-4}	6.3×10^{-5}	3.2×10^{-5}	4.6×10^{-5}	–
K_{fc}	0.2	0.2	0.2	0.2	–
K_{ic}	–	2.0×10^{-5}	1.2×10^{-5}	1.7×10^{-5}	1.0×10^{-3}
k_{1s}	–	15.0	15.0	15.0	15.0
k_{1f}	–	0.8	0.8	0.8	0.8
k_2	–	4.0	4.0	4.0	4.0

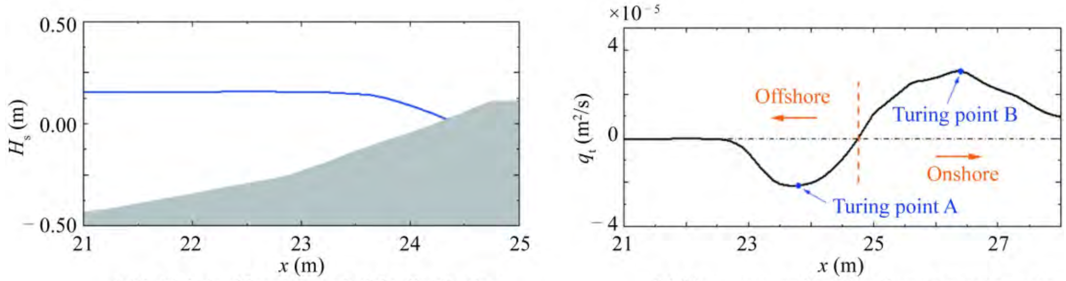

(a) Initial significant wave height distribution (c) Time-averaged total sediment transport rate

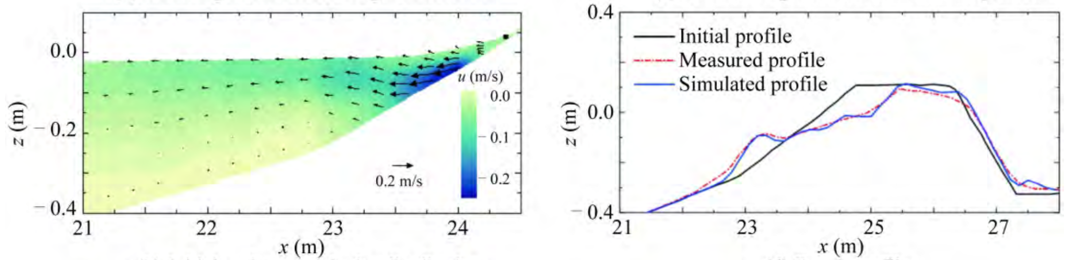

(b) Initial undertow velocity distribution (d) Beach profiles

Fig. 5. Case 1: simulated (a) initial significant wave height distribution, (b) initial undertow velocity distribution, and (c) time-averaged total sediment transport rate and (d) comparisons between the simulated (blue solid line) and measured (red dashed-dotted line) beach profiles.

Table 2 Performance statistics for the validation cases.

Case No.	Parameter	*RMSE* (m)	*CC*
1	Beach profile	0.015	0.997
2-BD	Significant wave height	0.018	0.988
	Mean water level	0.002	0.998
	Beach profile	0.013	0.992
2-WD	Beach profile	0.019	0.989
2-SD	Beach profile	0.012	0.993
3	Beach profile (along the flume centerline)	0.023	0.988
	Beach profile (normal to the flume centerline)	0.072	0.978

$$CC=\frac{\frac{1}{n}\sum_{i=1}^{n}[(x_i-\bar{x})(y_i-\bar{y})]}{\sqrt{\frac{1}{n}\sum_{i=1}^{n}(x_i-\bar{x})^2}\sqrt{\frac{1}{n}\sum_{i=1}^{n}(y_i-\bar{y})^2}}, \tag{38}$$

where n is the number of measured samples; x_i and y_i denote the calculated and measured values, respectively; and $\bar{x}$ and $\bar{y}$ are the corresponding mean values of the calculated and measured values, respectively. Table 2 presents the performance statistics for the validation cases. The *RMSE* between the simulated and measured beach profiles for Case 1 is rather small (0.015 m), while the correlation coefficient (*CC*) is 0.997. These results show that the established model can reasonably simulate onshore/offshore sediment transport and changes in the beach profile under the action of nearshore wave, undertow and RO.

3.2 Case 2: Both runup and inundation overwash

Figlus et al. (2009, 2011) conducted overwash (both RO and IO) experiments on dunes with different morphologies in the “Sand Tank” movable bed wave flume at the University of Delaware. The tank was 30.0 m long, 2.5 m wide, and 1.5 m deep. The water depth at the wave maker was approximately 1.0 m. H_s and T_p of the incident waves were 0.19 m and 2.6 s, respectively. Sediment with a d_{50} of 0.18 mm was used in the experiments to produce three different initial dune profiles, namely, a berm and a dune (BD), a wide dune (WD), and a sloping beach with a dune (SD). The wave breaker types are spilling breakers. A low-crested vertical wall was set on the onshore side of each dune. See Figlus et al. (2009) for the detailed experimental setup and morphological profile parameters.

Table 1 lists the value of each empirical coefficient used in our test. h_0 in the IO transport algorithm was set to the experimental water depth (1.0 m). The grid resolution is 0.2 m in the simulation. The time step is 0.002 s for FVCOM and 10 s for SWAN, and the coupling between the two models takes place at a 10 s interval.

Based on the morphological evolution characteristics, Figlus et al. (2011) divided the overwash process in each set of experiments into three phases (see Table 2 in Figlus et al. (2011)). Fig. 6 compares the simulated significant wave height H_s and mean water level η with measured data, taking the results at the end of Phase 1 for BD experiment as an example. As we can see, wave breaking occurs first at $x\approx$ 7.5 m and then a second time at $x\approx$ 17.5 m. The mean water level changes mainly in the nearshore zone. The decrease in H_s leads to a relatively significant wave setup. The model-calculated values are overall consistent with the measurements. The statistical measures show that the correlation coefficient (*CC*) values are larger than 0.98, while the values of *RMSE* for H_s and η are 0.018 m and 0.002 m, respectively (Table 2). At $x \approx 18.6$ m, the simulated H_s appears to be smaller than the measured data. This may be because that the measuring point is located in the intermittently wet and dry zone, which has some errors of measurement and data analysis (Figlus et al., 2009).

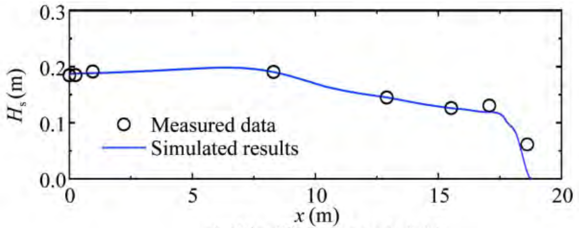

(a) Significant wave height

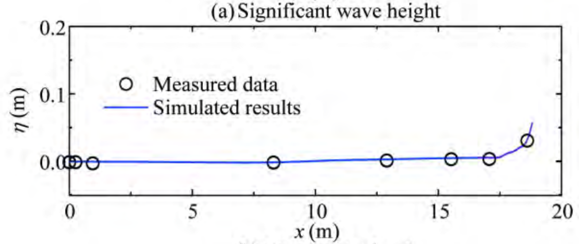

(b) Mean water level

Fig. 6. Case 2: comparisons between the simulated (blue solid line) and measured (black circle) significant wave height H_s and mean water level η at the end of Phase 1 for the BD test (t = 2400 s).

Fig. 7 compares the simulated and measured morphologies of the three dune profiles at the end of each phase. For the BD profile, during Phase 1 (0–2400 s), the nearshore sand berm and its onshore dune are eroded under wave-current and RO action, and the sediment composing the sand berm is transported offshore to be deposited at the toe of the sand berm ($x \approx 17.1$ m). Some sediment composing the sand berm and dune moves to the vicinity of the junction of the sand berm and the dune (at $x \approx 18.9$ m) under nearshore wave-current action. Because the nearshore dune is more affected by RO action, its sediment is transported onshore, resulting in a decrease in dune crest height z_C by approximately 6 cm. During Phase 2 (2400–3600 s), overwash transport intensifies to some extent. The nearshore morphology changes considerably within 1200 s. A small amount of sediment continues to move offshore, while the majority of the sediment is transported onshore under the action of wave overtopping. During Phase 3 (3600–7200 s), the dune crest begins to drop below the mean water level, giving way to IO. Then, the beach profile lowers, and the nearshore sand berm and dune are completely wiped away. The overall *RMSE* for this case is 0.013 m, and the correlation coefficient is 0.992, indicating that the model performs well at simulating the morphological changes in the BD profile.

Analysis of the simulated WD profile shows the following. During Phase 1 (0–1200 s), the foreslope of the dune is considerably eroded. A large amount of sediment is transported offshore from the foreslope of the dune under wave and undertow action and is deposited near the seaward toe of the dune ($x \approx 18.0$ m). In contrast, some sediment com-

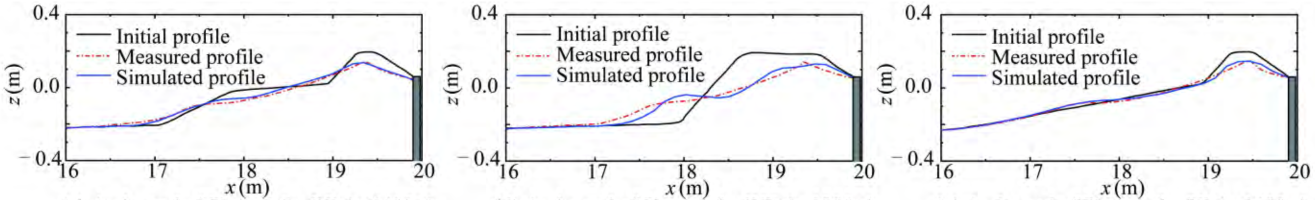

(a) At the end of Phase 1 for BD (t=2400 s) (d) At the end of Phase 1 for WD (t=1200 s) (g) At the end of Phase 1 for SD (t=1600 s)

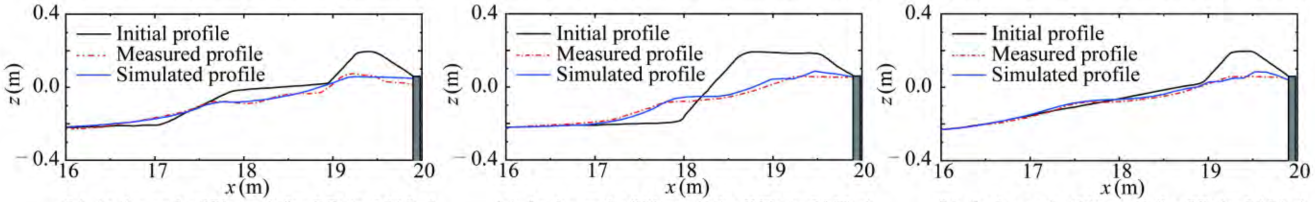

(b) At the end of Phase 2 for BD (t=3600 s) (e) At the end of Phase 2 for WD (t=2000 s) (h) At the end of Phase 2 for SD (t=2400 s)

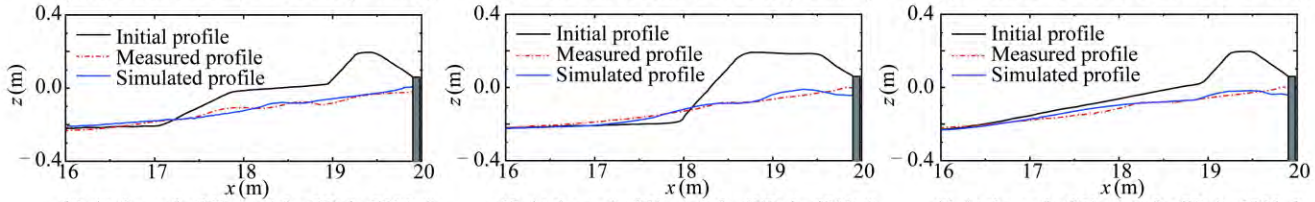

(c) At the end of Phase 3 for BD (t=7200 s) (f) At the end of Phase 3 for WD (t=4800 s) (i) At the end of Phase 3 for SD (t=6000 s)

Fig. 7. Case 2: comparisons between the simulated (blue solid line) and measured (red dashed-dotted line) beach profiles at the end of Phases 1 (top), 2 (middle), and 3 (bottom) for the BD (left), WD (middle) and SD (right) tests.

posing the crest and backslope side of the dune is transported onshore under RO action, resulting in a decrease in z_C by approximately 6 cm. During Phase 2 (1200–2000 s), the dune sediment continues to be transported onshore by the overtopping flow, resulting in a continual decrease in z_C. The nearshore morphology of the dune basically disappears at the end of Phase 2. During Phase 3 (2000–4800 s), the beach at the location where the dune used to stand continues to be overwashed, and its highest point begins to drop below the mean water level. Then, wave-dominated IO occurs, resulting in an overall descent of the beach profile in the zone at $x > 17.0$ m. The calculated bed level at $x > 19.5$ m at the end of Phase 3 is lower than the measurement, but overall, the model performs relatively well at simulating the profile changes under nearshore wave-current and overwash action. The correlation coefficient is 0.989, while *RMSE* is satisfactorily small (0.019 m).

For the SD profile, during Phase 1 (0–1600 s), a small amount of sediment in the zone at 18 m $< x <$ 19 m is transported offshore and is deposited at $x \approx 17.5$ m. The RO of the dune at 19 m $< x <$ 20 m leads to onshore sediment transport and reduces z_C by approximately 5 cm. During Phase 2 (1600–2400 s), RO transport intensifies considerably, and the nearshore dune vanishes basically within 800 s. During Phase 3 (2400–6000 s), the dune crest gradually drops below the mean water level, at which time the mode of overwash transitions from RO to IO, and subsequently, the beach profile lowers as a whole. Finally, the nearshore dune is completely erased. The model slightly underestimates the erosion of the beach at $x \approx 17.7$ m at the end of Phase 3. The simulated beach profile in the zone at $x > 19.6$ m is also slightly lower than the measurement. Nevertheless, as shown in Fig. 7 and Table 2, the model accurately captures the characteristics of the SD profile changes due to erosion and deposition and succeeds in simulating a relatively reasonable pattern of morphological changes.

Overall, once their empirical coefficients are appropriately adjusted, the overwash algorithms and numerical model established in this study perform well at simulating overwash-induced morphological changes in different profile forms, and they can reasonably describe their morphological erosion and deposition patterns during the RO and IO stages.

3.3 Case 3: Breaching induced by inundation overwash

This section presents simulations of IO and its resulting barrier breaching conducted based on the experiments of Wang et al. (2020), who used a wave flume that was 75.0 m long, 1.8 m wide, and 2.0 m deep. A trapezoidal sand barrier fabricated of sediment with a d_{50} of 1.2 mm was placed in the center of the flume. Both the foreslope and backslope of the barrier had a gradient of 1:4. An inverted trapezoidal pilot breach 0.36 m wide at the top edge, 0.10 m wide at the bottom edge, and 0.10 m deep was prepared in the barrier along the centerline of the flume. The water depth in front of the barrier was 0.85 m. Our simulations were performed based on the parameters used in Experiment 3 (height and period of incident waves of 0.16 m and 1.8 s, respectively), whose wave breaker type is plunging. See Wang et al. (2020) for the detailed experimental settings.

The experimental results obtained by Wang et al. (2020) showed that overwash-induced breaching was reflected mainly by the gradual expansion of the gap due to continual overwash at the gap under overtopping flow action. To characterize this feature, we provide an overwash-induced breach transport rate distribution equation based on the algorithm developed in Section 2.4.3:

$$q_{\mathrm{brc}}(x',\ y') = q_{\mathrm{c}}(x')\max\left[1-\left(\frac{|y'-y'_0|}{b_0+K_{\mathrm{br}}h_{\mathrm{br}}}\right)^{k_3},\ 0\right], \tag{39}$$

where x' and y' are the cross-shore and longshore coordinates, respectively; $q_{\mathrm{c}}(x')$ is the rate at which sediment is transported through the center of the gap in the cross-shore profile (calculated using the RO and IO transport algorithms established in Section 2.4.3); y'_0 is the longshore coordinate of the centerline of the breach gap; b_0 is the characteristic width of the breach gap (set to 1–2 times the maximum width of the initial gap, which is 0.5 m in this case); K_{br} is an empirical coefficient used to characterize the lateral breach velocity at the gap (set to 1.0); h_{br} is the depth of the breach gap at its centerline; and k_3 is an empirical coefficient used to represent the decrease in the sediment transport rate at the breach gap toward both sides (set to 3.0).

Table 1 summarizes the values of the empirical coefficients in the IO algorithm used in this case. Based on the experiment, h_0 was set to 0.85 m. The triangular mesh has a resolution of 0.2 m at the open boundary and is locally refined with a resolution of approximately 0.05 m in the vicinity of the pilot breach. Because of the high grid resolution, the time steps used for FVCOM and SWAN are 0.0002 s and 5 s, respectively, while the coupling between the two models takes place every 5 s.

Fig. 8 shows the initial topography and simulated breach topography at different time points. The initial gap continually deepens due to overwash and gradually expands to both sides. At $t = 198$ s, the barrier exhibits more significant morphological changes on its backslope ($x > 0.4$ m) (Fig. 8b), followed by the morphological evolution of its crest and foreslope (Figs. 8c and 8d). The model simulations are consistent with the overwash-induced breach characteristics described by Wang et al. (2020). Fig. 8 also shows that the rate of change of the morphology gradually slows with time.

Fig. 9 compares the simulated and measured profiles along the centerline of the flume at $t = 198$, 600, and 1198 s. The model simulations clearly illustrate that the IO-induced changes in the morphological profile of the barrier mainly

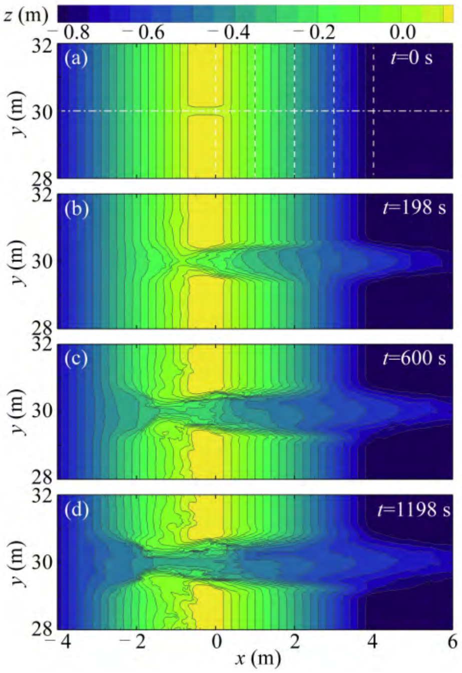

Fig. 8. Case 3: (a) initial topography and the simulated breach topography at (b) t = 198 s, (c) t = 600 s, and (d) t = 1198 s. The white dashed-dotted line is the validation profile along the flume centerline (y = 30 m), and the dashed lines are the validation profiles normal to the flume centerline.

begin from its backslope and then reach its crest and foreslope and that the profile of the eroded barrier displays an overall triangular shape. At t = 198 s, the sediment in the upper part of the barrier in the zone at x < 2.6 m is transported onshore by wave overtopping, while deposition occurs in the zone at x > 2.6 m. Overall, the simulated beach profile is relatively consistent with the measurements. At t = 600 s, the sediment at the foreslope side and crest of the barrier continues to move onshore under overtopping flow action and is deposited at x > 2.7 m. The simulation shows that at t = 1198 s, the main body of the barrier is further eroded, and deposition occurs at x > 2.9 m. Fig. 9 shows that the model-calculated deposition thickness is lower than the measurement but not to a significant extent. The difference between the simulated and measured profiles at each time point is mainly manifested on the foreslope side. The modeled erosion of the foreslope is more extensive than the measured erosion, which may be because the foreslope of the barrier was covered with a thin clay layer to prevent seepage in the flume experiment, which weakened the erosion by waves and currents. The statistical scores are $RMSE$ = 0.023 m and CC = 0.988 (Table 2), which show that the model basically succeeds in simulating the morphological profile changes along the centerline of the flume. The difference between the simulations and measurements is within reasonable limits.

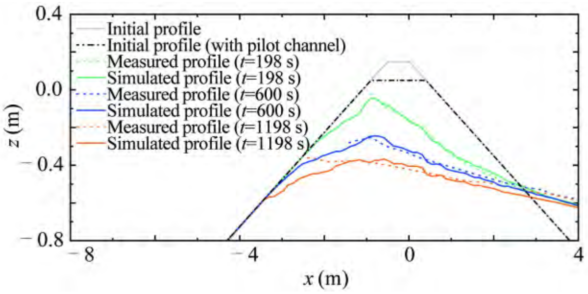

Fig. 9. Case 3: comparisons between the simulated (solid lines) and measured (dashed lines) beach profiles along the flume centerline (white dashed-dotted line in Fig. 8a) at t = 198 s (green lines), t = 600 s (blue lines), and t = 1198 s (orange lines).

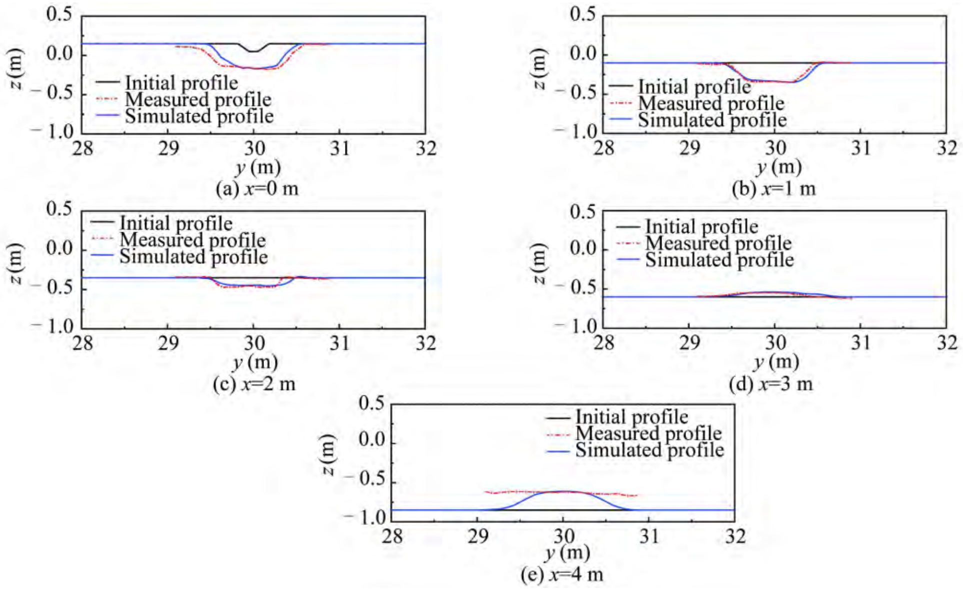

Fig. 10. Case 3: comparisons between the simulated (blue solid lines) and measured (red dashed-dotted lines) beach profiles normal to the flume centerline (white dashed lines in Fig. 8a) at t = 198 s.

Fig. 10 compares the simulated and measured profiles of the backslope perpendicular to the centerline of the flume at t = 198 s. The empirical algorithm established in this section (Eq. (39)) performs relatively well at calculating the overwash-induced breaching and the longshore morphological changes. The gap significantly deepens and widens at the sections at x = 0, 1, and 2 m. The gap formed from breaching basically maintains its trapezoidal shape. The profiles of x = 3 and 4 m rise to some extent at 29 m < y < 31 m, suggesting the occurrence of deposition in this zone. Overall, the simulated profiles at x = 0, 1, 2, and 3 m agree relatively well with the measurements. The simulated depths and widths of the gap created by breaching are relatively consistent with the measurements. The simulated profile at x = 4 m differs to some extent from the measurement, mainly in the smaller amount of sediment deposited on each side calculated by the model than that seen in the measurement. This difference occurs because the model does not account for the effects of the lateral flow spread on the morphology of both sides. The overall *RMSE* and *CC* for the profiles normal to the flume centerline are 0.072 m and 0.978, respectively, which are acceptable for a morphological model.

4 Sensitivity analysis of empirical coefficients

The overwash algorithms established in this study contain multiple empirical coefficients, which cover the effects of many complex factors, such as local hydrodynamic conditions, sediment properties, and beach profile morphologies. Theorizing on the value of each coefficient remains quite challenging. Therefore, the sensitivity of each empirical coefficient is comprehensively analyzed in this section based on the cases in Section 3 to summarize its pattern of influence.

4.1 Empirical coefficients in the runup overwash algorithm

$K_{\rm sc}$ and $K_{\rm dc}$ are the empirical coefficients of cross-shore sediment transport in the swash zone and in the barrier/dune crest zone, respectively, and they mainly control the magnitude of the RO-induced cross-shore sediment transport rate. According to the description in Section 2.4.3.1, setting $K_{\rm sc}$ equal to $K_{\rm dc}$ can ensure a continuous sediment transport rate at the junction of the swash and barrier/dune crest zones ($x' = x_3$ in Fig. 3). However, in practical applications, the model can be used to simulate different beach profile morphologies by setting these two coefficients to different values. Generally, in cases involving erosion of the dune crest (e.g., the cases in Sections 3.1 and 3.2), $K_{\rm dc}$ can be set higher than $K_{\rm sc}$.

Fig. 11 shows the time-averaged $q_{\rm t}$ values and beach profiles yielded by the model with different values of $K_{\rm sc}$ and $K_{\rm dc}$, holding the other coefficients constant (see Table 1) under the conditions in Case 1 as an example. The values of $K_{\rm sc}$ and $K_{\rm dc}$ mainly affect the magnitude and gradient of the sediment transport rate in the zone at x > 24 m. Relatively high values of $K_{\rm sc}$ and $K_{\rm dc}$ lead to pronounced dune erosion in the zone at 24 m < x < 25.5 m and a slightly large extent of deposition in the backslope zone at x > 26.4 m. We found that the values of $K_{\rm sc}$ and $K_{\rm dc}$ used in Case 1 are significantly higher than those in the other cases (Table 1). This difference occurs partly because the coefficient values include the effects of factors such as sediment properties and beach profile morphologies, and the other important reason is that the errors of the Stockdon et al. (2006) formulation used to estimate the wave runup height R need to be corrected by adjusting $K_{\rm sc}$ and $K_{\rm dc}$. Specifically, the value of R calculated by the Stockdon et al. (2006) formulation for Case 1 is nearly 0.17 m, while the estimated R for Case 2-WD is approximately 0.73 m due to the steep slope (1:2), which may be overestimated. The significant differences in the estimated runup heights in different cases lead to the $K_{\rm sc}$ and $K_{\rm dc}$ values in Case 1 being nearly an order of magnitude higher than those used in the other cases. Based on the results obtained from the cases examined in this study, $K_{\rm sc}$ and $K_{\rm dc}$ may generally be set to values on the order of 10^{-5}–10^{-4}.

The empirical coefficient of cross-shore sediment transport in the backslope zone $K_{\rm fc}$ mainly controls the distribution of the sediment transport rate in this region. Fig. 12 shows the time-averaged $q_{\rm t}$ values and morphological profile changes yielded by the model with different values of $K_{\rm fc}$ with Phase 1 of the overwash process involving the WD profile given in Case 2 (Case 2-WD) as an example. $q_{\rm t}$ in the zone at x < 18.7 m is mainly offshore and peaks at $x \approx$ 18.2 m, beyond which it gradually decreases. In contrast, $q_{\rm t}$ at x > 18.8 m is onshore. The value of $K_{\rm fc}$ mainly affects $q_{\rm t}$

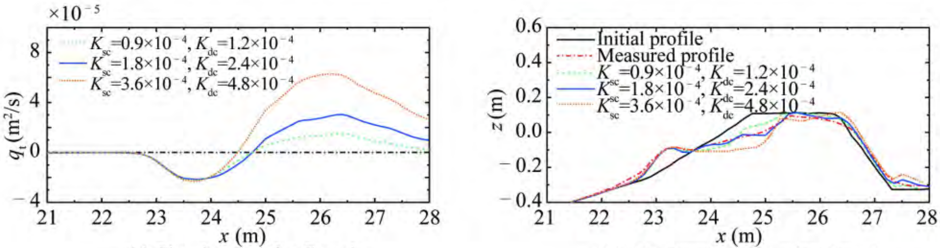

(a) Simulated $q_{\rm t}$ for Case 1

(b) Simulated profiles for Case 1

Fig. 11. Simulated (a) time-averaged total sediment transport rates $q_{\rm t}$ and (b) beach profiles for Case 1 with different values of $K_{\rm sc}$ and $K_{\rm dc}$.

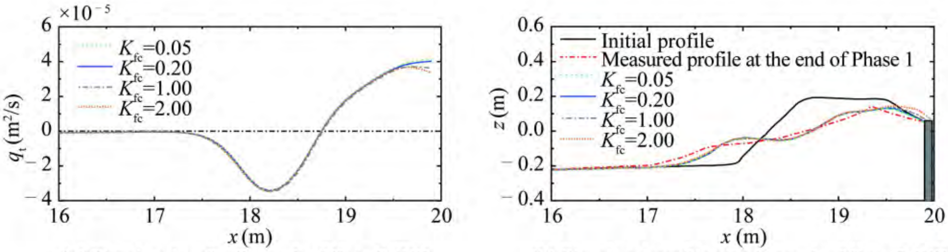

(a) Simulated q_t for Phase 1 of Case 2-WD (b) Simulated profiles for Phase 1 of Case 2-WD

Fig. 12. Simulated (a) time-averaged total sediment transport rates q_t and (b) beach profiles for Phase 1 of Case 2-WD with different values of K_{fc}.

and the morphology yielded by the model in the zone at $x >$ 19.6 m. The use of a relatively high value of K_{fc} in the model leads to a high rate of decrease in q_t in this zone as well as some extent of deposition. Moreover, as shown in Fig. 12, the final results yielded by the model with K_{fc} values of 0.05 and 0.2 are similar. Overall, the model results are less sensitive to K_{fc} than those to K_{sc} and K_{dc}. According to Table 1, K_{fc} of 0.2 or lower is generally recommended for cases involving the RO of relatively regular barriers.

4.2 Empirical coefficients in the inundation overwash algorithm

Figs. 13a and 13b show the effects of the cross-shore IO transport coefficient K_{ic} on the simulation of q_t and the morphological profile during Phase 3 of the overwash process involving the SD profile in Case 2 (Case 2-SD). A relatively high value of K_{ic} in the model leads to a high IO transport rate and, correspondingly, a large extent of erosion of the morphological profile. Based on the optimal values of the empirical coefficients for each case in Table 1, K_{ic} can be considered to be on the same order of magnitude as K_{sc} and K_{dc}. In the simulation of a process involving both modes of overwash (i.e., RO and IO) (e.g., Case 2), K_{ic} usually needs to be set lower than K_{sc} and K_{dc}. We preliminarily recommend that K_{ic} be set to a value of (0.4–0.6)K_{sc}.

Figs. 13c and 13d show the effects of K_{ic} on the calculation of the sediment transport rate and morphological profile, taking the simulation of the overwash process at 0–198 s in Case 3 as an example. The coefficient K_{ic} affects the overall magnitude of the IO transport rate, thereby affecting the extent to which the barrier is eroded. Simulations conducted with a relatively large value of K_{ic} show a more significant erosion of the barrier on both the foreslope and backslope sides. Compared with that for Case 2, the value of K_{ic} for Case 3, which involves a breaching process, is significantly higher (Table 1), mainly because the narrowing effects of the gap increase the intensity with which the flow passing through the gap overwashes the sediment. Based on the values of the coefficients selected for Case 3, we recommend that K_{ic} be set to a value on the order of 10^{-3} for the gap in simulations of an IO-induced breach. We believe that this pattern is also applicable to K_{sc} and K_{dc}. Therefore, we also recommend that K_{sc} and K_{dc} be set to values on the order of 10^{-3} for the gap in simulations of an RO event and its resulting breaching process.

Fig. 14 shows the time-averaged q_t values and morphological profile changes yielded by the model with different values of k_{1s}, taking Phase 3 of Case 2-BD as an example.

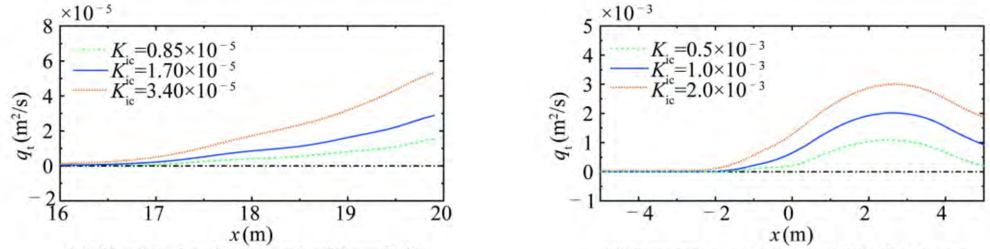

(a) Simulated q_t for Phase 3 of Case 2-SD (c) Simulated q_t within 0–198 s for Case 3

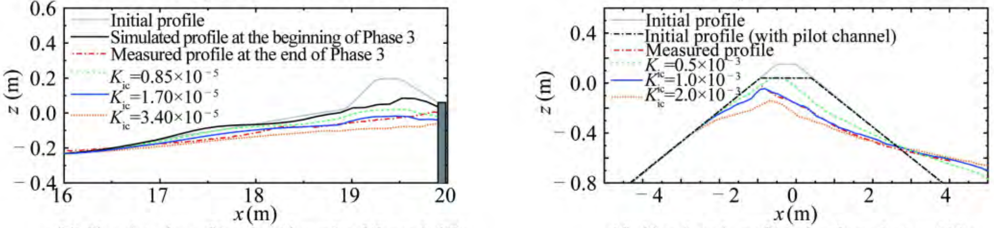

(b) Simulated profiles for Phase 3 of Case 2-SD (d) Simulated profiles for Case 3 at t=198 s

Fig. 13. Simulated (a) time-averaged total sediment transport rates q_t and (b) beach profiles for Phase 3 of Case 2-SD and simulated (c) time-averaged total sediment transport rates q_t within 0–198 s and (d) beach profiles at t = 198 s along the flume centerline for Case 3 with different values of K_{ic}.

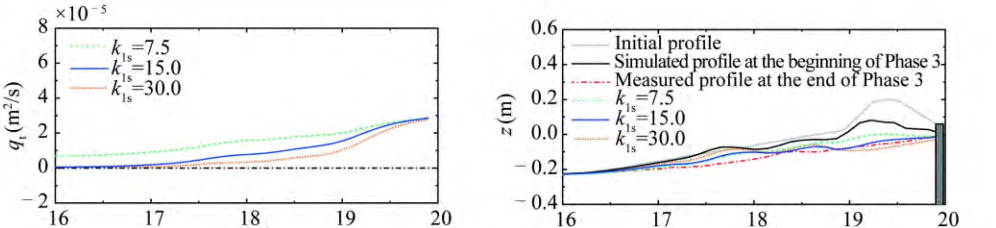

(a) Simulated q_t for Phase 3 of Case 2-BD (b) Simulated profiles for Phase 3 of Case 2-BD

Fig. 14. Simulated (a) time-averaged total sediment transport rates q_t and (b) beach profiles for Phase 3 of Case 2-BD with different values of k_{1s}.

The model-calculated gradient of q_t with k_{1s} = 7.5 is lower at 18 m < x < 20 m, resulting in a higher beach profile in this region. In the zone at x < 18 m, the morphological profile calculated with k_{1s} of 7.5 is slightly lower than that calculated with a k_{1s} of 15.0. At 18.8 m < x < 20 m, the q_t gradient calculated with k_{1s} of 30.0 is larger than that calculated with a k_{1s} of 15.0. As a result, inputting k_{1s} = 30.0 in the model produces a larger extent of erosion and a lower beach profile in this region. In the relatively offshore zone at x < 18.8 m, both q_t and its gradient calculated with k_{1s} of 30.0 are even lower, resulting in an even higher morphological profile.

The effects of k_{1f} on the simulations are analyzed in this section based on Case 3 (Fig. 15). The results yielded by the model with different values of k_{1f} differ considerably, especially on the landward side of the barrier. q_t yielded by the model with k_{1f} of 3.2 for the zone at x > –0.8 m first increases and then decreases but is relatively low in both value and gradient. As a result, the final beach profile simulated with k_{1f} = 3.2 is notably higher than the measurement and that simulated with k_{1f} = 0.8. Inputting k_{1f} = 0.2 in the model yields both higher q_t values and a steeper q_t gradient in the zone at x > –1.0 m, resulting in a larger extent of erosion and a lower beach profile than those simulated with k_{1f} of 0.8. The point of intersection of the profile simulated with k_{1f} of 0.2 and the initial profile is located at $x \approx 3.3$ m, where the peak of q_t occurs.

Overall, the coefficients k_{1s} and k_{1f} mainly affect the simulation of the distribution of q_t and the beach profile on the seaward and landward sides of the barrier crest, respectively. In the model simulations, higher values of k_{1s} result in higher erosion intensities within a small area on the seaward side of the barrier crest but smaller erosion areas, while smaller values of k_{1s} lead to lower erosion intensities on the seaward side of the barrier crest but larger erosion areas. A higher value of k_{1f} results in a relatively low erosion intensity on the landward side of the barrier crest. Moreover, k_{1f} somewhat affects the beach morphology (e.g., the backslope gradient) (Fig. 15b). Based on the simulation results obtained in this study and the values of the coefficients used in this study (Table 1), we recommend k_{1s} of 15.0 and k_{1f} of 0.8 for the model in practical applications.

Fig. 16 shows the effects of k_2 on the model calculations, taking the simulation results at different time points in Case 3 as an example. As the overwash process proceeds, there is a gradual decrease in q_t and its gradient along the profile, as well as in the overwash intensity. As shown in Figs. 16a and 16b, inputting different values of k_2 in the model produces similar q_t values in the period 0–198 s of the overwash process and highly consistent beach profiles at t = 198 s. This result occurs because of the small change in z_C during this period. Figs. 16c and 16d show the q_t values and beach profiles yielded by the model within 0–600 s. Inputting a smaller k_2 value in the model yields a relatively high q_t value and, correspondingly, a low beach profile. An opposite phenomenon is seen with a higher k_2 value. Figs. 16e and 16f also show this pattern.

As Fig. 16 shows, as the overwash process progresses and z_C decreases, the effects of k_2 on the final simulated profile become stronger. Based on the simulation results obtained for the cases examined in this study, we recommend k_2 of 4.0.

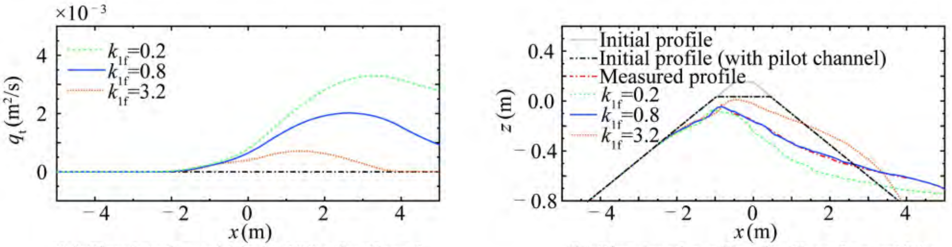

(a) Simulated q_t within 0−198 s for Case 3 (b) Simulated profiles for Case 3 at t=198 s

Fig. 15. Simulated (a) time-averaged total sediment transport rates q_t within 0–198 s and (b) beach profiles at t = 198 s along the flume centerline for Case 3 with different values of k_{1f}.

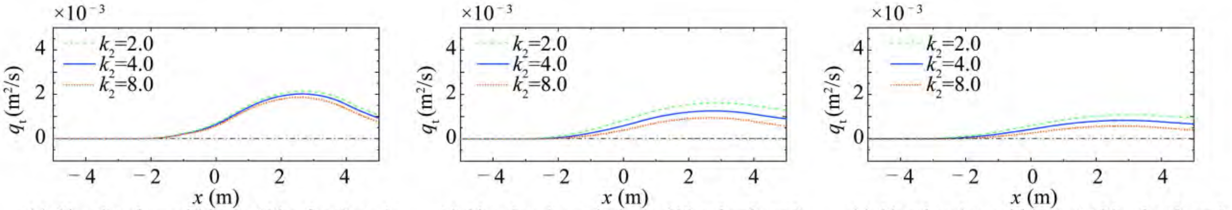

(a) Simulated q_t within 0−198 s for Case 3 (c) Simulated q_t within 0−600 s for Case 3 (e) Simulated q_t within 0−1198 s for Case 3

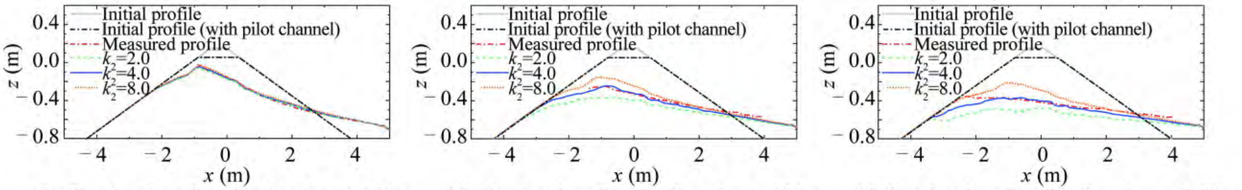

(b) Simulated profiles for Case 3 at t=198 s (d) Simulated profiles for Case 3 at t=600 s (f) Simulated profiles for Case 3 at t=1198 s

Fig. 16. Simulated time-averaged total sediment transport rates q_t within (a) 0–198 s, (c) 0–600 s, and (e) 0–1198 s and beach profiles at (b) t = 198 s, (d) 600 s, and (f) 1198 s along the flume centerline for Case 3 with different values of k_2.

5 Conclusions

In this study, a phase-averaged wave-current-sediment transport model that can simulate coastal overwash is established. Two overwash (RO and IO) transport algorithms are developed and introduced into the model. For the RO transport algorithm, the relevant coastal zone is divided into a swash zone, a barrier/dune crest zone, and a backslope zone. An empirical sediment transport equation is established to calculate the RO sediment transport rate in each zone. For the IO transport algorithm, the relationship between the sediment transport rate and the beach profile height is established. The IO transport rate across the profile is calculated using different parametric values for the seaward and landward sides of the dune crest.

The established model is validated against the data obtained from three sets of laboratory experiments (i.e., RO experiments, overwash experiments involving the whole RO and IO process, and IO and resulting breaching experiments). The validation results and statistical analyses show that the model established in this study can satisfactorily simulate the overwash-induced beach profile changes and the erosion and deposition evolution processes under different conditions.

The sensitivity analysis of each empirical coefficient in the overwash transport algorithms reveals that satisfactory simulation results can be produced with the recommended values for the majority of the coefficients, including $K_{\mathrm{fc}} = 0.2$, $k_{1\mathrm{s}} = 15.0$, $k_{1\mathrm{f}} = 0.8$, and $k_2 = 4.0$. The other three coefficients (K_{sc}, K_{dc}, and K_{ic}) mainly control the magnitude of the sediment transport rate and may require appropriate adjustment in practical simulations. Based on the simulated results obtained in this study for multiple cases, the RO transport coefficients K_{sc} and K_{dc} can usually be set to values on the order of 10^{-5}–10^{-4}, while under the same conditions, the IO transport coefficient K_{ic} can be preliminarily set to (0.4–0.6)K_{sc}. In the event of a breach, the narrowing effects of the breach gap increase the overwash intensity. Therefore, K_{sc}, K_{dc}, and K_{ic} should be set to much higher values. We recommend values on the order of 10^{-3} for these three coefficients at the gap locations.

Although overwash transport algorithms for the cross-shore and longshore directions have been developed for the model established in this study, the model has only been validated against laboratory data in the areas of beach profiles whose evolution is dominated by cross-shore overwash transport. The capability of the model to simulate in situ overwash in a large area and the empirical coefficients of longshore sediment transport are the focus of our future research.

Acknowledgment

The authors gratefully acknowledge Prof. HE Zhi-guo for sharing his experimental data.

Right and permissions

References

Booij, N., Ris, R.C. and Holthuijsen, L.H., 1999. A third-generation wave model for coastal regions: 1. Model description and validation, *Journal of Geophysical Research: Oceans*, 104(C4), 7649–7666.

Cao, Z.X., Hu, P., Li, W. and Li , J., 2021. *Mechanics of Sediment Transport*, China Water & Power Press, Beijing. (in Chinese)

Cao, Z.B., Zhang, C., Chi, S.H., Zhuang, L. and Zheng, J.H., 2020. Video-based monitoring of an artificial beach nourishment project, *Journal of Coastal Research*, 95(SI), 1037–1041.

Carruthers, E.A., Lane, D.P., Evans, R.L., Donnelly, J.P. and Ashton, A.D., 2013. Quantifying overwash flux in barrier systems: An example from Martha's Vineyard, Massachusetts, USA, *Marine Geology*, 343, 15–28.

Chen, C.S., Huang, H.S., Beardsley, R.C., Liu, H.D., Xu, Q.C. and Cowles, G., 2007. A finite volume numerical approach for coastal ocean circulation studies: Comparisons with finite difference models, *Journal of Geophysical Research*: *Oceans*, 112(C3), C03018.

Chen, C.S., Liu, H.D. and Beardsley, R.C., 2003. An unstructured grid, finite-volume, three-dimensional, primitive equations ocean model: Application to coastal ocean and estuaries, *Journal of Atmospheric and Oceanic Technology*, 20(1), 159–186.

Chen, T.Q., Zhang, Q.H., Wu, Y.S., Ji, C., Yang, J.S. and Liu, G.W., 2018. Development of a wave-current model through coupling of FVCOM and SWAN, *Ocean Engineering*, 164, 443–454.

Deng, X.H., Liu, H.J., Jiang, Z.L. and Baldock, T.E., 2016. Swash flow properties with bottom resistance based on the method of characteristics, *Coastal Engineering*, 114, 25–34.

Donnelly, C., 2008. *Coastal Overwash*: *Processes and Modelling*, Ph.D. thesis, Lund University, Sweden.

Donnelly, C., Kraus, N.C. and Larson, M., 2006. State of knowledge on measurement and modeling of coastal overwash, *Journal of Coastal Research*, 22(4), 965–991.

Figlus, J., Kobayashi, N., Gralher, C. and Iranzo, V., 2009. *Experimental and Numerical Study on the Transition from Minor to Major Overwash of Dunes*, Center for Applied Coastal Research, University of Delaware, Newark, DE.

Figlus, J., Kobayashi, N., Gralher, C. and Iranzo, V., 2011. Wave overtopping and overwash of dunes, *Journal of Waterway, Port, Coastal, and Ocean Engineering*, 137(1), 26–33.

Goda, Y., 2009. A performance test of nearshore wave height prediction with CLASH datasets, *Coastal Engineering*, 56(3), 220–229.

Hancock, M.W. and Kobayashi, N., 1994. Wave overtopping and sediment transport over dunes, *Proceedings of the 24th International Conference on Coastal Engineering*, ASCE, Kobe, pp. 2028–2042.

Harris, B.D., Johnson, C., Jafari, N.H., Chen, Q. and Ozdemir, C.E., 2020. Effects of coupled consolidation and overwash processes on a low-lying headland system, *Coastal Engineering*, 160, 103746.

Hu, P., Li, W., He, Z.G., Pähtz, T. and Yue, Z.Y., 2015. Well-balanced and flexible morphological modeling of swash hydrodynamics and sediment transport, *Coastal Engineering*, 96, 27–37.

Ji, C., Zhang, Q.H. and Wu, Y.S., 2017. Derivation of three-dimensional radiation stress based on lagrangian solutions of progressive waves, *Journal of Physical Oceanography*, 47(11), 2829–2842.

Ji, C., Zhang, Q.H. and Wu, Y.S., 2018. An empirical formula for maximum wave setup based on a coupled wave-current model, *Ocean Engineering*, 147, 215–226.

Ji, C., Zhang, Q.H. and Wu, Y.S., 2019. A comparison study of three-dimensional radiation stress formulations, *Coastal Engineering Journal*, 61(2), 224–240.

Kobayashi, N., 2013. *Cross-Shore Numerical Model CSHORE 2013 for Sand Beaches and Coastal Structures*, Center for Applied Coastal Research, University of Delaware, Newark, DE.

Kobayashi, N., 2016. Coastal sediment transport modeling for engineering applications, *Journal of Waterway, Port, Coastal, and Ocean Engineering*, 142(6), 03116001.

Kupfer, S., Ferreira, Ó. and Costas, S., 2020. Assessment of overwash-induced flooding at two beaches along the southwest Algarve, Portugal, *Journal of Coastal Research*, 95(SI), 484–489.

Larson, M. and Kraus, N.C., 1989. *SBEACH*: *Numerical Model for Simulating Storm-Induced Beach Change*, *Report 1*: *Empirical Foundation and Model Development*, US Army Engineer Waterways Experiment Station, Coastal Engineering Research Center, Vicksburg, MS.

Larson, M., Kubota, S. and Erikson, L., 2004a. Swash-zone sediment transport and foreshore evolution: Field experiments and mathematical modeling, *Marine Geology*, 212(1-4), 61–79.

Larson, M. and Wamsley, T.V., 2007. A formula for longshore sediment transport in the swash, *Proceedings of Coastal Sediments '07*, ASCE, New Orleans, LA, pp. 1924–1937.

Larson, M., Wise, R.A. and Kraus, N.C., 2004b. *Coastal Overwash, Part 2*: *Upgrade to SBEACH*, US Army Engineer Research and Development Center, Coastal and Hydraulics Laboratory, Vicksburg, MS.

Lesser, G.R., Roelvink, J.A., van Kester, J.A.T.M. and Stelling, G.S., 2004. Development and validation of a three-dimensional morphological model, *Coastal Engineering*, 51(8–9), 883–915.

Li, W., Hu, P., Pähtz, T., He, Z.G. and Cao, Z.X., 2017. Limitations of empirical sediment transport formulas for shallow water and their consequences for swash zone modelling, *Journal of Hydraulic Research*, 55(1), 114–120.

Madsen, O.S., 1991. Mechanics of cohesionless sediment transport in coastal waters, *Proceedings of Coastal Sediments '91*, ASCE, Seattle, WA, pp. 15–27.

Matias, A, Ferreira, Ó., Vila-Concejo, A., Morris, B. and Dias, J.A., 2010. Short-term morphodynamics of non-storm overwash, *Marine Geology*, 274(1–4), 69–84.

Matias, A, Masselink, G., Kroon, A., Blenkinsopp, C.E. and Turner, I.L., 2013. Overwash experiment on a sandy barrier, *Journal of Coastal Research*, 65(SI), 778–783.

Matias, A., Williams, J.J., Masselink, G. and Ferreira, Ó., 2012. Overwash threshold for gravel barriers, *Coastal Engineering*, 63, 48–61.

McCall, R.T., Masselink, G., Poate, T.G., Roelvink, J.A., Almeida, L.P., Davidson, M. and Russell, P.E., 2014. Modelling storm hydrodynamics on gravel beaches with XBeach-G, *Coastal Engineering*, 91, 231–250.

McCall, R.T., van Thiel de Vries, J.S.M., Plant, N.G., van Dongeren, A.R., Roelvink, J.A., Thompson, D.M. and Reniers, A.J.H.M., 2010. Two-dimensional time dependent hurricane overwash and erosion modeling at Santa Rosa Island, *Coastal Engineering*, 57(7), 668–683.

Park, Y.H., 2006. *Overwash Induced by Storm Conditions*, Ph.D. thesis, Texas A&M University, College Station, TX.

Roelvink, D., Reniers, A., van Dongeren, A., van Thiel de Vries, J., McCall, R. and Lescinski, J., 2009. Modelling storm impacts on beaches, dunes and barrier islands, *Coastal Engineering*, 56(11–12), 1133–1152.

Soulsby, R.L., 1997. *Dynamics of Marine Sands*: *A Manual for Practical Applications*, Thomas Telford Publications, London.

Soulsby, R.L. and Damgaard, J.S., 2005. Bedload sediment transport in coastal waters, *Coastal Engineering*, 52(8), 673–689.

Srinivas, R. and Dean, R.G., 1996. Cross-shore hydrodynamics and profile response modeling, *Coastal Engineering*, 27(3–4), 195–221.

Stockdon, H.F., Doran, K.S. and Sallenger Jr., A.H., 2009. Extraction of lidar-based dune-crest elevations for use in examining the vulnerability of beaches to inundation during hurricanes, *Journal of Coastal Research*, 53(SI), 59–65.

Stockdon, H.F., Holman, R.A., Howd, P.A. and Sallenger, A.H., 2006. Empirical parameterization of setup, swash, and runup, *Coastal Engineering*, 53(7), 573–588.

Svendsen, I.A., 1984. Wave heights and set-up in a surf zone, *Coastal Engineering*, 8(4), 303–329.

van Dongeren, A., Roelvink, D., McCall, R., Nederhoff, K. and van Rooijen, A., 2017. Modeling the morphological impacts of coastal storms, in: Ciavola, P. and Coco, G. (eds.), *Coastal Storms: Processes and Impacts*, John Wiley & Sons, Ltd., Chichester, pp. 195–216.

van Rijn, L.C., 1993. *Principles of Sediment Transport in Rivers, Estuaries and Coastal Seas*, Aqua Publications, The Netherlands.

van Rijn, L.C., 2007. Unified view of sediment transport by currents and waves. Ⅱ: Suspended transport, *Journal of Hydraulic Engineering*, 133(6), 668–689.

Wang, Y.Q., Xu, D., He, Z.G. and Wu, W.M., 2020. Experimental study on sand dike breaching by wave overtopping, *Applied Ocean Research*, 101, 102195.

Zhu, F.F. and Dodd, N., 2013. Net beach change in the swash zone: A numerical investigation, *Advances in Water Resources*, 53, 12–22.